

Monolayer VTe₂: incommensurate Fermi-surface nesting and suppression of charge density wave

Katsuki Sugawara,^{1,2,3} Yuki Nakata,¹ Kazuki Fujii,¹ Kosuke Nakayama,¹

Seigo Souma,^{2,3} Takashi Takahashi,^{1,2,3} and Takafumi Sato^{1,2,3}

¹*Department of Physics, Tohoku University, Sendai 980-8578, Japan*

²*Center for Spintronics Research Network, Tohoku University, Sendai 980-8577, Japan and*

³*WPI Research Center, Advanced Institute for Materials Research, Tohoku University, Sendai 980-8577, Japan*

(Dated: April 8, 2024)

We investigated the electronic structure of monolayer VTe₂ grown on bilayer graphene by angle-resolved photoemission spectroscopy (ARPES). We found that monolayer VTe₂ takes the octahedral 1T structure in contrast to the monoclinic one in the bulk, as evidenced by the good agreement in the Fermi-surface topology between ARPES results and first-principles band calculations for octahedral monolayer 1T-VTe₂. We have revealed that monolayer 1T-VTe₂ at low temperature is characterized by a metallic state whereas the nesting condition is better than that of isostructural monolayer VSe₂ which undergoes a CDW transition to insulator at low temperature. The present result suggests an importance of Fermi-surface topology for characterizing the CDW properties of monolayer TMDs.

Layered transition-metal dichalcogenides (TMDs) are a promising candidate for realizing outstanding properties associated with two-dimensionalization since bulk TMDs are known to exhibit various physical properties such as magnetism, Mott-insulator phase, and charge density wave (CDW), besides the wide range of transport property (insulator, semiconductor, metal, and superconductor), most of which are prone to the change in the dimensionality of materials. When TMDs are thinned to a single monolayer (2D limit), they exhibit even more outstanding properties distinct from bulk, as represented by the room-temperature ferromagnetism in VSe₂ in contrast to the nonmagnetic nature of bulk [1] and the change in the band-gap property from indirect to direct transition in MoS₂ [2]. The CDW is a most pronounced phenomenon widely seen in both bulk and atomic-layer TMDs. In bulk TMDs, the interplay between the Fermi-surface nesting and the energy-gap opening as well as its relationship to the strength of CDW properties such as the CDW transition temperature (T_{CDW}) has been a target of intensive studies [3].

The role of dimensionality to the mechanism of CDW, in particular whether or not the CDW is more stable in the 2D limit, is now becoming a target of fierce debates, being stimulated by a recent success in fabricating various atomic-layer TMDs by exfoliation and epitaxial techniques. Recent studies on some TMDs such as TiSe₂, VSe₂, and NbSe₂ [4–8] have shown a marked increase in T_{CDW} upon reducing the thickness down to a few monolayers. In contrast, it has been reported that the CDW vanishes in monolayer TaS₂ and TaSe₂ [9, 10], suggesting an important role of substrate and many-body effects. In 1T-VSe₂, reducing the number of layers by exfoliating bulk crystal leads at first to gradual decrease of T_{CDW} , but at a critical film thickness of ~ 10 nm, the T_{CDW} exhibits a characteristic upturn and reaches 140 K in a few monolayers, much higher than bulk T_{CDW} (110 K) [11]. Such enhancement of T_{CDW} in monolayer VSe₂ was also

revealed by angle-resolved photoemission spectroscopy (ARPES) wherein the role of FS nesting and electron-phonon coupling was intensively debated [4, 6, 7, 12–14]. However, the nature of 2D CDW is still far from reaching a consensus, as highlighted by a wide variety of periodic lattice distortions hitherto proposed for monolayer VSe₂ (e.g., 4×4 , 4×1 , $\sqrt{7} \times \sqrt{3}$, $4 \times \sqrt{3}$) [6, 7, 12–14]. In a broader perspective, it is still unclear to what extent the conventional FS-nesting picture can be applied to the 2D CDW materials and how the FS topology and electronic interactions are related to the CDW properties such as the enhancement/suppression of T_{CDW} . To address these essential questions, a further study on the electronic structure with new monolayer TMDs is highly required.

In this Rapid Communication, we report a successful fabrication of monolayer VTe₂ on bilayer graphene / SiC and its ARPES investigation. While the monoclinic (1T^m) phase is known to be stable in bulk VTe₂, our monolayer VTe₂ film takes the octahedral 1T structure [see Fig. 1(a)]. Importantly, this enables us to directly compare the electronic states and CDW properties with isostructural monolayer 1T-VSe₂. Our ARPES study on monolayer VTe₂ signifies a large, nearly perfectly nested triangular FS centered at the K point in the Brillouin zone (BZ). We also found that the V 3d band apparently crosses the Fermi level (E_{F}) midway between the Γ and K points, indicative of the metallic state at low temperature, unlike monolayer VSe₂ which shows a fully gaped insulating state below 140 K. We discuss possible origins for such an intriguing difference in terms of the variation in the FS-nesting condition and electron-phonon coupling.

A high-quality monolayer VTe₂ film was grown on bilayer graphene by the molecular-beam-epitaxy (MBE) method. ARPES measurements were performed at the BL-28B beamline in Photon Factory, KEK. First-principles band-structure calculations were carried out

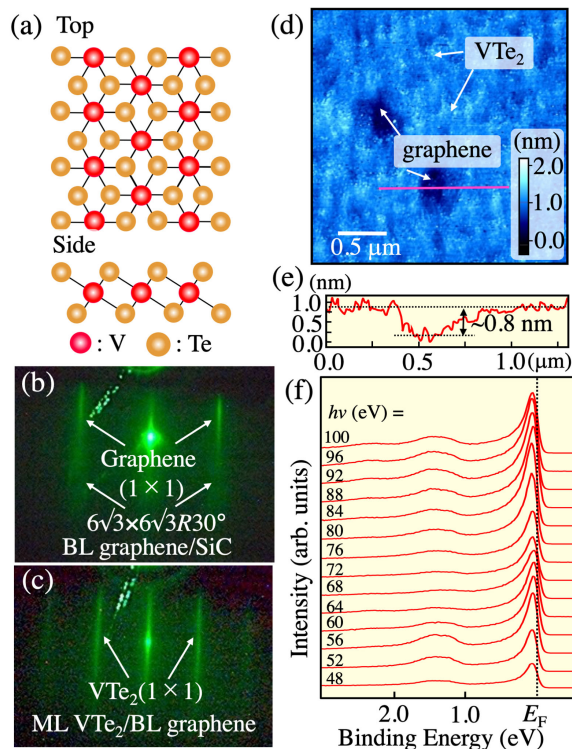


FIG. 1. (a) Crystal structure of monolayer $1T$ -VTe₂. (b),(c) RHEED patterns of bilayer (BL) graphene and monolayer (ML) VTe₂ on BL graphene, respectively. (d) AFM image of monolayer VTe₂. High (white), medium (blue), and low (dark) intensity regions are attributed to atoms/molecules adsorbed on VTe₂, clean monolayer VTe₂, and atoms molecules adsorbed on graphene substrate, respectively. The reason why we did not attribute the dominant white and blue areas to graphene or 2 monolayer VTe₂ is because we performed *in-situ* ARPES measurements with the same sample and observed a dominant contribution from the monolayer energy bands to the total ARPES intensity. (e) Height profile along a cut shown by magenta solid line in (d). (f) Photon-energy dependence of the EDC at the Γ point in monolayer VTe₂.

using the QUANTUM ESPRESSO code with generalized gradient approximation [15, 16]. For details, see section 1 of Supplemental Material [17].

First, we present characterization of monolayer VTe₂ film. Figure 1(b) shows the reflection high-energy electron diffraction (RHEED) pattern of pristine bilayer graphene on SiC(0001) substrate. We clearly observe the 1×1 and $6\sqrt{3} \times 6\sqrt{3} R30^\circ$ streak patterns, which correspond to bilayer graphene and underlying carbon-mesh layer on SiC, respectively [18]. After growing a VTe₂ film by co-depositing V and Te atoms onto the bilayer-graphene surface, the RHEED intensity from the substrate disappears, and a sharp 1×1 streak pattern appears [Fig. 1(c)], similarly to the case of other monolayer TMD films grown on bilayer graphene [6, 19, 20], indicating the formation of VTe₂. Absence of additional streak patterns suggests no inclusion of monoclinic phase with

zigzag chain structure which is known to exist in bulk VTe₂ below 482 K [21, 22]. This situation is particularly suited for comparing the electronic states with other $1T$ monolayer polymorphs. We come back to this point later in detail. As seen in the *ex-situ* atomic force microscopy (AFM) image in Fig. 1(d), large islands with a typical height of 0.8 nm, which corresponds to that of monolayer [Fig. 1(e)], are recognized on bilayer graphene. The energy distribution curve (EDC) at the Γ point in Fig. 1(f) signifies no detectable photon-energy ($h\nu$) variation in the energy position of bands, supporting the 2D nature of electronic states.

We have estimated the in-plane lattice constant of monolayer VTe₂ as $a \sim 3.35$ Å at room temperature by comparing the relative position of the RHEED patterns between graphene and VTe₂. This value is in good agreement with that estimated from the absolute wave vector values at the M (1.08 ± 0.03 Å⁻¹) and K (1.24 ± 0.03 Å⁻¹) points relative to the Γ point in the ARPES data (3.35 ± 0.09 Å). (including error bars due to the angular resolution and the angle-to- \mathbf{k} conversion). Intriguingly, these values are much smaller than that of bulk octahedral $1T$ -VTe₂ (3.64 Å; obtained above 482 K where the $1T$ phase is stable). Taking into account that the coupling between graphene and $1T$ -VTe₂ film could be sufficiently weak due to the van-der-Waals-coupling nature, it is inferred that the value of 3.35 Å could be the most stable lattice parameter for free-standing monolayer VTe₂.

Figures 2(a) and 2(b) display the plot of valence-band ARPES intensity for monolayer VTe₂ measured at $T = 40$ K along the ΓM and ΓK cuts with $h\nu = 56$ eV, compared with the corresponding band dispersion obtained by the first-principles band-structure calculations for free-standing monolayer $1T$ -VTe₂ with the input of experimental lattice constant a . One can see in Fig. 2(a) several energy bands whose dispersion appears to be symmetric with respect to the Γ point. A side-by-side comparison of Figs. 2(a) and 2(b) also reveals a good agreement in the overall valence-band structure between the experiment and calculations, demonstrating that the fabricated monolayer VTe₂ indeed takes the $1T$ structure (see section 2 of Supplemental Material for details [17]). According to the calculations, energy bands lying at the binding energy (E_B) of 1-6 eV, including the hole-like bands which rapidly move toward E_F on approaching the Γ point, are attributed to the Te $5p$ orbitals, while the energy band within 0.5 eV of E_F with a relatively flat dispersion around the M point is assigned as the V $3d$ band.

To see more clearly the electronic states responsible for the physical properties, we show in Figs. 2(c) and 2(d) the ARPES intensity near E_F at $T = 40$ K measured along the ΓM and ΓK cuts, respectively. A detailed spectral analysis by tracing the peak position of EDCs suggests that two topmost Te $5p$ bands with dif-

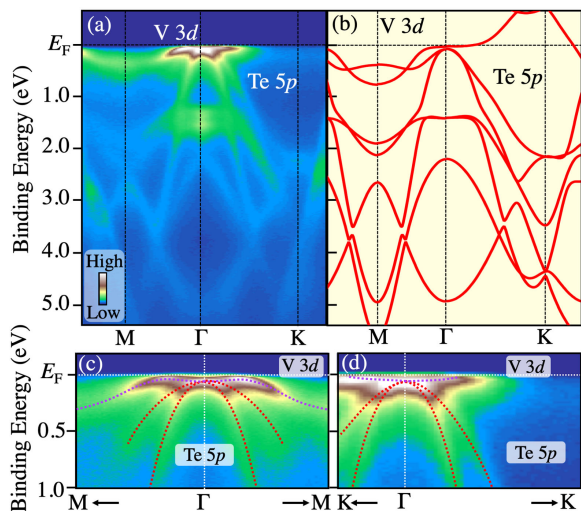


FIG. 2. (a) Plot of ARPES intensity for monolayer VTe_2 along the ΓM and ΓK cuts measured with $h\nu = 56$ eV at $T = 40$ K. (b) Band structure obtained from the first-principles band-structure calculations for monolayer 1T-VTe_2 with the input of experimental in-plane lattice constant (3.35 Å). Overall calculated bands were contracted by 13 % in the energy axis to find a reasonable matching with the experiment. (c),(d) Experimental band structure near E_F , measured along the ΓM and ΓK cuts, respectively. Red and purple dashed curves are a guide for the eyes to trace the Te $5p$ and V $3d$ bands, respectively.

ferent band velocities do not reach E_F , but are topped at 60 meV below E_F at the Γ point. These bands are degenerate exactly at the Γ point, consistent with the calculation in Fig. 2(b). We found that the shallow V $3d$ band is also located at ~ 60 meV below E_F at the Γ point and disperses toward higher E_B on approaching the M point [Fig. 2(c)], while it crosses E_F midway between the Γ and K points, accompanied with a sudden drop in the spectral weight [Fig. 2(d)]. While the overall experimental band structure shows a good agreement with the calculated band structure for the 1T phase, we found that some bands near E_F in the experiment are renormalized with respect to those in the calculations (for details, see section 2 of Supplemental Material [17]). It is noted here that we found no evidence for the energy splitting of bands associated with possible exchange splitting due to ferromagnetism, which is further corroborated by our x-ray magnetic circular dichroism measurement at 80 K showing no change in the V $L_{2,3}$ -absorption edge across the magnetic-field reversal [23]. This suggests the absence of ferromagnetic order in monolayer VTe_2 . At this stage, it is unclear why the ferromagnetism appears in monolayer VSe_2 but not in monolayer VTe_2 , though it is noted that the ferromagnetism in monolayer VSe_2 itself is contradictory and is currently a target of fierce debate [1, 6, 7]. It is also unknown whether or not the ferromagnetic property is related to the CDW.

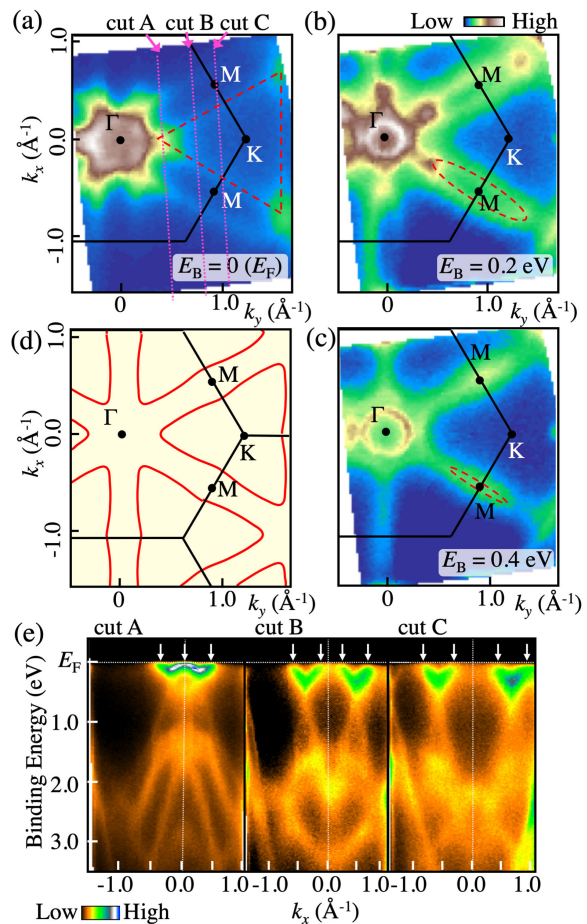


FIG. 3. (a)-(c) Plots of ARPES intensity at $T = 40$ K as a function of 2D wave vector, k_x and k_y , at three representative energy slices at $E_B = E_F$, 0.2 eV, and 0.4 eV, respectively. Energy contours were obtained by integrating the intensity within ± 50 meV with respect to each E_B 's. (d) Calculated FS obtained from the first-principles band-structure calculations for monolayer 1T-VTe_2 . (e) ARPES-derived band structure along three representative \mathbf{k} cuts [cuts A-C in (a)] which cross the triangular FS. The systematic evolution of the V-shaped band dispersions from cut A to cut C indicates the holelike nature of triangular FS.

To clarify the topology of FS, we have performed ARPES measurements in 2D \mathbf{k} space. Figures 3(a)-3(c) show the contour maps of ARPES intensity for different E_B slices. At $E_B = E_F$ [Fig. 3(a)], one can recognize a couple of fairly straight intensity patterns around the M point running parallel to the ΓM direction (red dashed line). This intensity pattern forms a large, almost perfectly triangular-shaped FS enclosing the K point. Remarkably, this FS is well reproduced by the calculations for free-standing 1T-VTe_2 [Fig. 3(d)] with the input of experimental lattice constant, confirming again the 1T nature of our epitaxial film. Absence of any spurious intensity that could be associated with the band folding with (3×1) periodicity expected from the formation of

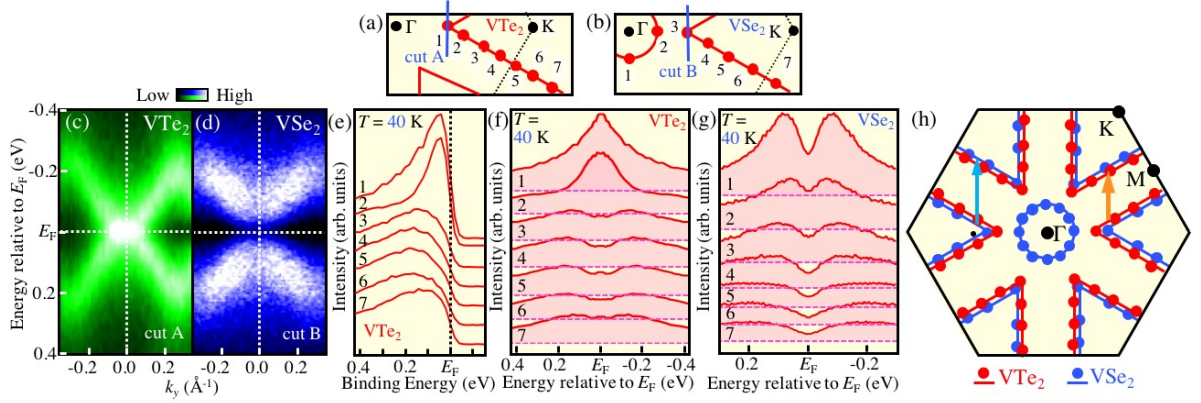


FIG. 4. (a),(b) Schematic FS together with a \mathbf{k} cut and \mathbf{k} points where high-resolution ARPES measurements were performed for monolayer VTe₂ and VSe₂, respectively. (c),(d) Plots of ARPES intensity as a function of wave vector and E_B symmetrized with respect to E_F , measured at $T = 40$ K along a cut crossing the corner of triangular pocket (cut A/B) for monolayer VTe₂ and VSe₂, respectively. (e) EDCs near E_F at $T = 40$ K for monolayer VTe₂ measured at various k_F points in (a). (f) Same as (e) but symmetrized with respect to E_F . Zero intensity for each spectrum is indicated by a dashed magenta line to highlight the absolute spectral weight. (g) Same as (f) but for monolayer VSe₂ [6]. (h) Comparison of the FS topology between monolayer VTe₂ and VSe₂. Red and blue circles correspond to the k_F points for monolayer VTe₂ and VSe₂, respectively. Orange and light blue arrows indicate possible nesting vectors q for monolayer VTe₂ and VSe₂, respectively.

double zigzag-chain superstructure seen in bulk VTe₂ [22] further corroborates the purely 1T nature of the film (see section 4 of Supplemental Material for details [17]).

Upon increasing E_B to 0.2 eV [Fig. 3(b)], the experimental triangular pattern seen at $E_B = 0$ eV [Fig. 3(a)] transforms into a M-point-centered ellipsoid elongated along the ΓM direction, which shrinks on further increasing E_B to 0.4 eV [Fig. 3(c)]. This indicates that the triangular FS forms a hole pocket, consistent with the calculated band dispersion in Fig. 2(b) in which the V $3d$ band is located at ~ 1 eV above E_F at the K point. Figure 3(e) shows the ARPES-derived band structure along three representative k cuts (cuts A-C) which cross the triangular FS. On cut A which touches the corner of triangular FS, one can see a couple of V-shaped bands in the vicinity of E_F . These two V-shaped bands are gradually separated from each other on going from cut A to cuts B and C, indicating that the triangular FS is holelike. In Figs. 3(b) and 3(c), one can also identify an intense circular spot at the Γ point stemming from the Te $5p$ bands. We emphasize again that although the proximity of Te $5p$ bands to E_F enhances the intensity at the Γ point, these fully occupied bands do not participate in the FS. Therefore, the FS of monolayer VTe₂ is solely dictated by the triangular hole pocket at the K point, which greatly simplifies the discussion on the FS topology and nesting, as detailed later. We have estimated the total carrier concentration to be 0.98 ± 0.08 electrons / unit cell, by evaluating the area of FS with respect to that of whole BZ. This suggests that our monolayer film keeps stoichiometry and no observable charge transfer from the substrate takes place.

Now that the FS topology is established, we shall address a key question regarding a possible energy gap opening associated with the occurrence of CDW. We selected a \mathbf{k} cut passing the corner of triangular FS [blue line in Fig. 4(a)], and show the ARPES intensity at $T = 40$ K plotted as a function of wave vector and E_B symmetrized with respect to E_F in Fig. 4(c). One can clearly see a dispersive band reaching E_F showing the brightest intensity at E_F , indicating the absence of an energy gap. This is in sharp contrast to the result of monolayer VSe₂ [Figs. 4(b) and 4(d)] that signifies a marked suppression of intensity within ± 0.1 eV of E_F at $T = 40$ K due to the CDW-gap opening [6]. To see the low-energy spectral feature in more detail, we have performed high-resolution ARPES measurements along several cuts crossing the FS, and show the EDCs at various k_F (Fermi wave vector) points (points 1-7) covering the whole straight segment of the triangular FS in the first BZ in Fig. 4(e). The corresponding symmetrized EDCs in Fig. 4(f) show a single peak at points 1 and 2 located around the corner of FS, while the EDCs at points 3-7 exhibit a weak dip structure at E_F indicative of a large residual spectral weight at E_F . We attribute this spectral-weight suppression as the pseudogap, but not the CDW gap, since the spectral behavior resembles that of monolayer VSe₂ at room temperature (well above $T_{CDW} \sim 140$ K), which shows the coexistence of pseudogap and metallic Fermi-arc states [6]. Also, the pseudogap of VTe₂ persists over a wide temperature range (10 - 300 K), similarly to VSe₂. It is noted that the pseudogap is unlikely to be due to some extrinsic effects such as the sample/surface quality and/or the experimental conditions (e.g. photoioniza-

tion cross-section and light polarization), but is an intrinsic feature of monolayer VTe₂. The pseudogap may be explained in terms of the CDW fluctuations and/or the electron-phonon coupling associated with the CDW (see also section 3 of Supplemental Material [17]). The metallic state revealed in Figs. 4(c) and 4(e) in VTe₂ is obviously different from the fully gapped insulating state below T_{CDW} , as visible from the strong spectral-weight suppression around E_F over the entire FS as seen in Fig. 4(g). We thus conclude that the CDW is suppressed in monolayer VTe₂.

A key to understand such a contrasting behavior may lie on the difference in the FS topology between the two V-dichalcogenide monolayers. Figure 4(h) directly compares the FS obtained from ARPES measurements of monolayer VTe₂ and VSe₂ [6]. One can immediately recognize that both monolayers show a similar triangular pocket at the K point whereas a circular hole pocket exists only in VSe₂. Extra hole carriers at the Γ -centered pocket in VSe₂ resides on the K-centered pocket in VTe₂, as seen from a larger triangular pocket in VTe₂. This is reasonable since the Se and Te atoms are isovalent and the total FS area should be the same. The expansion of triangular pocket would widen the straight segment of the FS in VTe₂. Assuming that the nesting vector q is parallel to the ΓM direction [6], this would lead to an enhancement of electronic susceptibility in VTe₂. Thus, one would naively expect that the CDW in VTe₂ is more stable than that in VSe₂ according merely to the FS-nesting picture. However, this is not the case since the CDW appears to be suppressed in VTe₂. Thus, one cannot sufficiently describe the CDW of monolayer VSe₂ or VTe₂ simply in terms of the energy gain around E_F in the electronic system, which suggests the importance of considering the electron-phonon coupling [24]. While detailed discussion on the relevance of electron-phonon coupling requires sophisticated first-principles band-structure calculations, we point out here a possibility that such an electron-phonon coupling could be linked to the electronic states via the commensurability of the nesting. We found that the nesting vector along the ΓM direction in VSe₂ is commensurate to the lattice ($1/4 \mathbf{G}$ where \mathbf{G} is the reciprocal lattice vector) [6], while that in VTe₂ is incommensurate ($1/4.6 \mathbf{G}$). If such commensurability enhances the electron-phonon coupling at the corresponding lattice periodicity, it may stabilize the CDW. However, this explanation is still speculative, requiring further experimental and theoretical studies to firmly pin down the CDW origin.

Our band calculations of monolayer VTe₂ show that a small (1.5 %) change in the in-plane lattice constant is sufficient to control the emergence/absence of a small hole pocket at Γ and the concomitant change in the FS-nesting condition at the triangular pocket. Such sensitivity of the FS topology to the lattice parameters is essential due to the fact that the narrow V $3d$ band is located

in the vicinity of E_F . Therefore, we expect that small perturbations such as lattice strain and carrier doping would easily trigger the change in the FS topology and the nesting vector, leading to the modulation of CDW properties. In this regard, the reported differences in the FS topology around the Γ point in VSe₂, which may link to diverse periodic lattice distortions [4, 6, 7, 13], may be interpreted in terms of a reflection of the high sensitivity of the CDW characteristics to the strain and carrier balance. The present result suggests an importance of precisely controlling the lattice strain and carrier concentration for manipulating the CDW. Such band engineering would be a main target of future studies.

In conclusion, we have performed an ARPES study on monolayer 1T-VTe₂ grown on bilayer graphene by MBE. We found a large triangular FS at the K point that satisfies a nearly perfect nesting condition, whereas the CDW is suppressed as highlighted by the observation of E_F -crossing of bands at low temperature, in contrast to monolayer VSe₂ that exhibits a well-defined CDW characterized by the fully gapped insulating state. The present result opens a pathway toward controlling novel physical properties of 2D TMDs through the band engineering.

We thank Y. Umemoto, K. Horiba, and H. Kumigashira for their assistance in the ARPES experiments. This work was supported by the MEXT of Japan (Innovative Area “Topological Materials Science” JP15H05853), JST-PREST (No. JPMJPR18L7), JST-CREST (No. JPMJCR18T1), JSPS KAKENHI Grants (No. JP18K18986, JP18H01821, JP18H01160, JP17H04847 and JP17H01139), KEK-PF (Proposal No. 2018S2-001), Science research projects from Murata Science Foundation, World Premier International Research Center, Advanced Institute for Materials Research. Y. N. acknowledges support from GP-Spin at Tohoku University.

-
- [1] M. Bonilla, S. Kolekar, Y. Ma, H. C. Diaz, V. Kalappattil, R. Das, T. Eggers, H. R. Gutierrez, M. -H. Phan, M. Batzill, *Nature Nanotech.* **13**, 289 (2018).
 - [2] K. F. Mak, C. Lee, J. Hone, J. Shan, and T. F. Heinz, *Phys. Rev. Lett.* **105**, 136805 (2010).
 - [3] K. Rossnagel, *J. Phys.: Condens. Matter* **23**, 213001 (2011).
 - [4] P. Chen, Y.-H. Chan, X.-Y. Fang, Y. Zhang, M. Y. Chou, S.-K. Mo, Z. Hussain, A.-V. Fedorov, and T. -C. Ching, *Nature Commun.* **16**, 8943 (2015).
 - [5] K. Sugawara, Y. Nakata, R. Shimizu, P. Han, T. Hito-sugi, T. Sato, and T. Takahashi, *ACS Nano* **10**, 1341 (2016).
 - [6] Y. Umemoto, K. Sugawara, Y. Nakata, T. Takahashi, and T. Sato, *Nano Res.* **12**, 165 (2018).
 - [7] J. Feng, D. Biswas, A. Rajan, M. D. Watson, F. Mazzola, O. J. Clark, K. Underwood, I. Marković, M. McLaren, A.

- Hunter, D. M. Burn, L. B. Duffy, S. Barua, G. Balakrishnan, F. Bertran, P. Le Fèvre, T. K. Kim, G. van der Laan, T. Hesjedal, P. Wahl, and P. D. C. King, *Nano Lett.* **18**, 4493 (2018).
- [8] X. Xi, L. Zhao, Z. Wang, H. Berger, L. Forró, J. Shan, and K. F. Mak, *Nature Nanotech.* **10**, 765 (2015).
- [9] C. E. Sanders, M. Dendzik, A. S. Ngankeu, A. Eich, A. Bruix, M. Bianchi, J. A. Miwa, B. Hammer, A. A. Khajetoorians, and P. Hofmann, *Phys. Rev. B.* **94**, 081404(R) (2016).
- [10] B. Shao, A. Eich, A. S. Ngankeu, M. Bianchi, P. Hofmann, A. A. Khajetoorians, and T. O. Wehling, *Nature Commun.* **10**, 180 (2019).
- [11] J. Yang, W. Wang, Y. Liu, H. Du, W. Ning, G. Zheng, C. Jin, Y. Han, N. Wang, Z. Yang, M. Tian, and Y. Zhang, *Appl. Phys. Lett.* **105**, 063109 (2014).
- [12] P. Chen, Woei Wu Pai, Y.-H. Chan, V. Madhavan, M. Y. Chou, S.-K. Mo, A.-V. Fedorov, and T.-C. Chiang, *Phys. Rev. Lett.* **121**, 196402 (2018).
- [13] G. Duvjir, B. K. Choi, I. Jang, S. Ulstrup, S. Kang, T. T. Ly, S. Kim, Y. H. Choi, C. Jozwiak, A. Bostwick, E. Rotenberg, J.-G. Park, R. Sankar, K.-S. Kim, J. Kim, and Y. J. Chang, *Nano Lett.* **18**, 5432 (2018).
- [14] D. Zhang, J. Ha, H. Baek, Y.-H. Chan, F. D. Natterer, A. F. Myers, J. D. Schumacher, W. G. Cullen, A. V. Davydov, Y. Kuk, M. Y. Chou, N. B. Zhitenev, and J. A. Stroscio, *Phys. Rev. Materials* **1**, 024005 (2017).
- [15] P. Giannozzi, S. Baroni, N. Bonini, M. Calandra, R. Car, C. Cavazzoni, D. Ceresoli, G. L. Chiarotti, M. Cococcioni, I. Dabo, A. D. Corso, S. de Gironcoli, S. Fabris, G. Fratesi, R. Gebauer, U. Gerstmann, C. Gougoussis, A. Kokalj, M. Lazzeri, L. Martin-Samos, N. Marzari, F. Mauri, R. Mazzarello, S. Paolini, A. Pasquarello, L. Paulatto, C. Sbraccia, S. Scandolo, G. Sclauszero, A. P. Seitsonen, A. Smogunov, P. Umari, and R. M. Wentzcovitch, *J. Phys. Condens. Matter* **21**, 395502 (2009).
- [16] J. P. Perdew, K. Burke, and M. Ernzerhof, *Phys. Rev. Lett.* **77**, 3865 (1996).
- [17] See Supplemental Material at [URL] for the details of experiment, band calculation, pseudogap origin, and possibility of monoclinic phase.
- [18] K. V. Emtsev, F. Speck, Th. Seyller, L. Ley, and J. D. Riley, *Phys. Rev. B* **77**, 155303 (2008).
- [19] K. Sugawara, T. Sato, Y. Tanaka, S. Souma, and T. Takahashi, *Appl. Phys. Lett.* **107**, 071601 (2015).
- [20] Y. Nakata, K. Sugawara, R. Shimizu, Y. Okada, P. Han, T. Hitosugi, K. Ueno, T. Sato, and T. Takahashi, *NPG Asia Mater.* **8**, e321 (2016).
- [21] K. D. Bronsema, G. W. Bus, and G. A. Wiegers, *J. Solid State Chem.* **53**, 415 (1984).
- [22] T. Ohtani, K. Hayashi, M. Nakahira, and H. Nozaki, *Solid State Commun.* **40**, 629 (1981).
- [23] Y. Nakata *et al.*, (unpublished).
- [24] M. Calandra, I. I. Mazin, and F. Mauri, *Phys. Rev. B* **80**, 241108(R) (2009).